Multiple Solar Sail Formation Flying Around Heliocentric Displaced Orbit via Consensus

Wei Wang[(1)], Alessandro A. Quarta[(2)], Giovanni Mengali[(2)*], Jianping Yuan[(1)]

[(1)] *National Key Laboratory of Aerospace Flight Dynamics, Northwestern Polytechnical University, 710072 Xi'an, People's Republic of China*

[(2)] *Department of Civil and Industrial Engineering, University of Pisa, I-56122 Pisa, Italy*

Abstract

This paper investigates the problem of multiple solar sail-based spacecraft formation flying in which the chief follows a heliocentric displaced orbit, whereas each deputy adjusts the sail propulsive acceleration so as to track a desired (relative) trajectory with respect to the chief. In particular, coordinated control strategies are presented for both the full state feedback case and the relative velocity unavailability case, respectively. The developed consensus-based algorithms rely on the protocols formulated on an undirected communication topology with information link couplings, utilizing every available neighbor-to-neighbor information data such that the reliability of the formation system can be enhanced. Illustrative examples show the validity the proposed method.

Keywords: Solar sail, Formation flying, Heliocentric displaced orbit, Consensus control

Nomenclature

a	=	semimajor axis, [au]
$\boldsymbol{a}$	=	propulsive acceleration, [mm/s^2]
e	=	eccentricity
$\boldsymbol{e}$	=	relative position errors [m]
$\mathcal{E}$	=	set of edges
f	=	true anomaly, [rad]
$\mathcal{G}$	=	communication topology graph
$\mathbb{I}$	=	identity matrix
H	=	displacement, [au]
$\mathbb{L}$	=	Laplacian matrix (with entries $[l_{ij}]$)
N	=	number of deputy spacecraft
n	=	mean motion, [rad/day]
n_r	=	angular velocity of reference relative orbit, [rad/day]
$\hat{\boldsymbol{n}}$	=	solar sail normal unit vector
O	=	Sun's center-of-mass
o	=	focus of displaced orbit
R	=	focus-spacecraft distance [au]
$\boldsymbol{r}$	=	position vector (with $r = \|\boldsymbol{r}\|$), [au]
S	=	solar sail

*Corresponding author

Email addresses: 418362467@qq.com (Wei Wang[(1)]), a.quarta@ing.unipi.it (Alessandro A. Quarta[(2)]), g.mengali@ing.unipi.it (Giovanni Mengali[(2)]), jyuan@nwpu.edu.cn (Jianping Yuan[(1)])

Published in Acta Astronautica, Vol. 154 January 2019, pp. 256–267. doi: http://dx.doi.org/10.1016/j.actaastro.2018.03.039

t	=	time, [days]
$\mathcal{T}_P$	=	perifocal frame
$\mathcal{T}_R$	=	rotating frame
u	=	reflectivity modulation ratio
$\boldsymbol{u}$	=	control input of deputy spacecraft
$\mathcal{V}$	=	set of vertices
$\hat{\boldsymbol{x}}$, $\hat{\boldsymbol{y}}$, $\hat{\boldsymbol{z}}$	=	unit vectors of coordinate axes
$\mathbb{W}$	=	weighted adjacency matrix (with entries $[w_{ij}]$)
α	=	cone angle, [rad]
β	=	lightness number
γ	=	elevation angle, [rad]
θ, φ	=	attitude angles [rad]
$\mu_\odot$	=	Sun's gravitational parameter, [$\mathrm{au}^3/\mathrm{day}^2$]
ρ_x, ρ_y, ρ_z	=	components of relative position vector in chief's rotating frame, [km]
$\boldsymbol{\rho}$	=	relative position vector, [km]
υ	=	vertex
$\boldsymbol{\omega}$	=	angular velocity (with $\omega = \|\boldsymbol{\omega}\|$), [rad/s]

Subscripts

P	=	planet
C	=	chief
i	=	i-th deputy
max	=	maximum
$\odot$	=	Sun

Superscripts

T	=	transpose
$\star$	=	reference value
$\cdot$	=	time derivative
$\wedge$	=	unit vector

1. Introduction

Over the last decades, solar sailing has been considered one of the most promising technologies for space mission application, such as interplanetary transfers [1, 2, 3, 4] and astronomical observations [5, 6], due to its remarkable advantages compared to more conventional propulsion systems. Unlike traditional spacecraft propelled by chemical or electric thrusters, a solar sail-based spacecraft exploits the solar radiation pressure to generate a continuous (low) thrust by the interaction of solar photons with a large reflecting surface. The peculiar propulsion mechanism of a solar sail enables the fulfilment of a class of high-energy orbits [7] as, for example, rectilinear trajectories [8, 9, 10], or closed orbits whose orbital plane does not contain the primary body [11]. Those non-Keplerian trajectories may be circular (or elliptic) heliocentric displaced orbits capable of observing the polar region of a celestial body [12], or quasi-periodic orbits around artificial Lagrange points [13], useful for monitoring solar plasma storms.

Some scientific tasks, such as the GeoSail magnetosphere mission [14, 15], require a continuous multi-aspect observation and a high-imaging resolution, thus necessitating the deployment of multiple spacecraft in a formation, so as to constitute a (virtual) synthetic aperture radar. In fact, by distributing the payload among multiple spacecraft while each one carries the indispensable functional modules only, a mass decrease (and size reduction) may be achieved for a single spacecraft, thereby significantly improving the system performance in terms of propulsive acceleration. In this context, the concept of solar sail formation flying has been proposed in some mission scenarios [16, 17]. Most of the available literature involving spacecraft formation flying is focused on a classical chief-deputy architecture, where the information data flows from

the chief to each deputy, without any mutual negotiation among deputies. One inherent weakness of such a chief-deputy topology is that the whole system is not able to effectively respond to unexpected situations or risks, since the chief is a single point of failure for the whole system [18]. In case of chief malfunction or when a fault takes place in the chief-deputy communication links, the whole mission is at risk of failure.

A possible solution to this problem consists in incorporating the deputy-to-deputy information exchange into the feedback control system, so as to increase the group robustness. This approach has been recently proposed by Wang et al. [19] in a context different from that discussed in this paper. More precisely, the formation flying problem presented in Ref. [19] involves electric solar wind sail-based spacecraft [20, 21], i.e. a propulsion system that is substantially different from a solar sail and, more importantly, the relative velocity of each neighboring spacecraft is assumed to be exactly known.

The aim of this paper is to present a distributed solar sail formation architecture around a heliocentric displaced orbit via a consensus concept. The coordinated cooperative control algorithms are used for solar sail formation maintenance, where each deputy adjusts its sail attitude and reflectivity modulation ratio so as to follow a prescribed relative geometry with respect to the chief. By exploiting the available neighbor-to-neighbor information data, the underlying consensus concept facilitates each deputy spacecraft to update its state in a cooperative way, (i.e., using information taken from its local neighbors) in such a way that the final tracking error of each spacecraft converges to zero. The paper also discusses the case in which the relative velocity information from the neighbor is not available. In this sense, the approach discussed in this work improves the model described in Ref. [19].

The paper is organized as follows. Section 2 investigates the conditions of generating a heliocentric, elliptic, displaced orbit for a solar sail-based spacecraft equipped with a reflectivity control device, and discusses the feasible regions for a given set of orbital parameters. Section 3 analyzes the mathematical model of the relative dynamics for solar sail formation flying around a heliocentric displaced orbit, which is then used as a basis for designing consensus-based distributed control algorithms in Section 4. The effectiveness of the control system is illustrated in Section 5 by means of some numerical simulations. Finally, some concluding remarks are given in Section 6.

2. Mathematical model

Consider a mission scenario in which multiple solar sail-based spacecraft, flying in formation, provide a continuous observation of the polar region of a celestial body as, for example, a planet (subscript P). Using the heliocentric (Keplerian) trajectory of the planet as the reference orbit of eccentricity e_P, introduce a perifocal reference frame $\mathcal{T}_P(O; \hat{\boldsymbol{x}}_P, \hat{\boldsymbol{y}}_P, \hat{\boldsymbol{z}}_P)$, in which the origin O is at the Sun's center-of-mass, the plane $(\hat{\boldsymbol{x}}_P, \hat{\boldsymbol{y}}_P)$ coincides with the planet orbital plane $\mathcal{P}$, axis $\hat{\boldsymbol{x}}_P$ points to the perihelion, and $\hat{\boldsymbol{z}}_P$ is positive in the direction of the planet angular momentum vector $\boldsymbol{\omega}_P$, see Fig. 1.

2.1. Conditions for maintaining an elliptic displaced orbit

In order to observe the polar region of the planet, the chief spacecraft (subscript C) covers an elliptic displaced orbit of semimajor axis a_C and eccentricity e_C, whose orbital plane is parallel to $\mathcal{P}$ and is displaced at a constant distance H_C (with respect to $\mathcal{P}$), see Fig. 1. The displaced orbit is maintained by exploiting a reflectivity control device (RCD) [22, 23], whose mathematical model is consistent with that proposed in Ref. [24]. More precisely, the sail surface can be thought of as being constituted by two parts. The first one is covered with high reflectivity material for which a specular reflection model without degradation [25, 26] is assumed (i.e., an ideal force model), whereas the second part is covered by a number of electrochromic material panels (EMPs) that are used to modulate the propulsive acceleration modulus within a suitable (small) range, see Fig. 2.

Each EMP is able to vary its reflectivity as a function of the applied voltage and, in a simplified analysis, when the EMP is in its power-on mode the solar photons are specularly reflected, whereas in power-off mode the incoming photons are totally absorbed. Note that this behaviour is consistent with the simplified mathematical model discussed in Ref. [24]. In order to avoid the introduction of additional torque on the spacecraft, it is assumed that a symmetry exists in the distribution of switched on/off panels with respect to the vehicle center of mass. Considering the generic solar sail-based spacecraft of the formation architecture, let the total sail area be denoted by A_s, while A_p is the sail area covered with EMPs. It is useful to introduce the reflectivity modulation ratio $u \triangleq A_{\text{off}}/A_s$, where A_{off} is the area of the switched-off panels calculated at

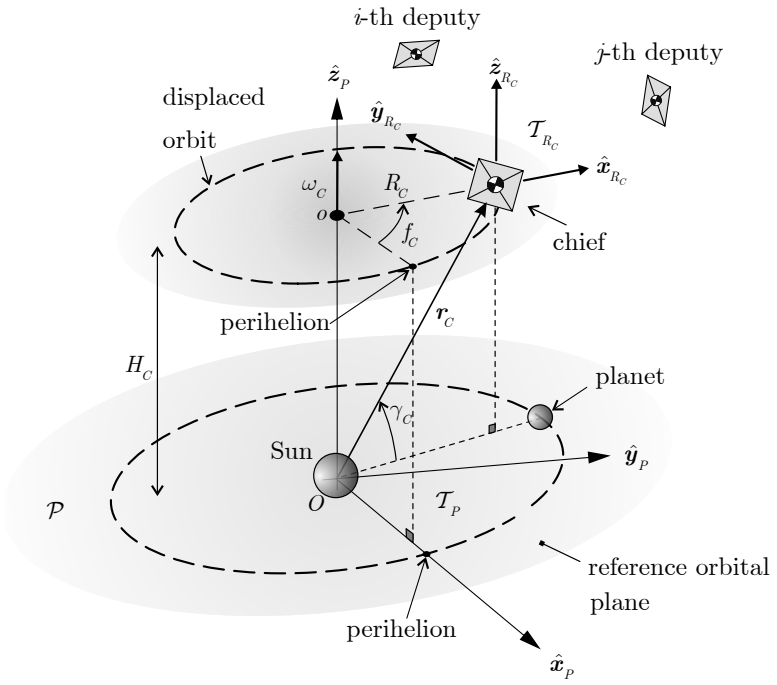

Figure 1: Reference frames.

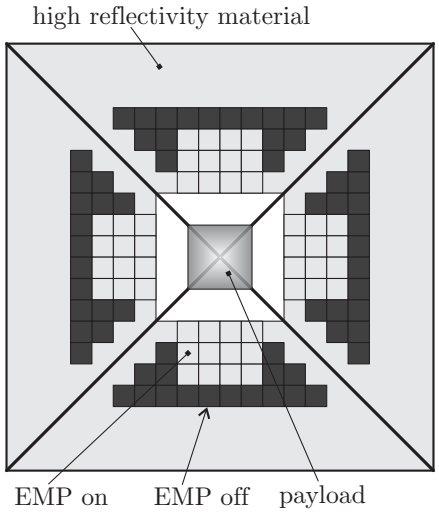

Figure 2: Conceptual scheme of a solar sail with electrochromic material panels.

a given time instant [24]. Accordingly, the range of the reflectivity modulation ratio is $u \in [0, u_{\max}]$, where $u_{\max} = A_p/A_s$ corresponds to the case where all of EMPs are in power-off mode. In particular, the ratio u is assumed to be varied with continuity, within its admissible range, by modulating the amount of on/off time of EMP devices.

For a continuous polar region observation, the chief orbital angular velocity ($\boldsymbol{\omega}_C$) and eccentricity (e_C) should match those of the planet, that is, $\boldsymbol{\omega}_C = \boldsymbol{\omega}_P$ and $e_C = e_P$. As a result, the chief lies, at any given time, in the same vertical plane passing through $\hat{\boldsymbol{z}}_P$ and containing the planet. According to Ref. [27], a heliocentric displaced orbit with such an arrangement is referred to as Planet Following Displaced Orbit (PFDO). Figure 1 also shows a second reference frame $\mathcal{T}_{R_C}(o; \hat{\boldsymbol{x}}_{R_C}, \hat{\boldsymbol{y}}_{R_C}, \hat{\boldsymbol{z}}_{R_C})$, that is, a chief-fixed rotating

frame in which $\hat{\boldsymbol{x}}_{R_C}$ is directed from the focus o of the displaced orbit to the chief spacecraft, while $\hat{\boldsymbol{z}}_{R_C}$ is along the direction of $\boldsymbol{\omega}_C$, that is, the direction of $\hat{\boldsymbol{z}}_{R_C}$ is orthogonal to the (displaced) orbital plane.

The equation of motion of the chief spacecraft in the rotating reference frame $\mathcal{T}_{R_C}$ can be written as [28]

$$\ddot{\boldsymbol{r}}_C + 2\,\boldsymbol{\omega}_C \times \dot{\boldsymbol{r}}_C + \dot{\boldsymbol{\omega}}_C \times \boldsymbol{r}_C + \boldsymbol{\omega}_C \times (\boldsymbol{\omega}_C \times \boldsymbol{r}_C) = -\frac{\mu_\odot}{r_C^3}\,\boldsymbol{r}_C + \boldsymbol{a}_C \tag{1}$$

where $\boldsymbol{a}_C$ is the solar sail propulsive acceleration, $\mu_\odot$ is the Sun's gravitational parameter, and $\boldsymbol{r}_C$ is the Sun-chief vector (with $r_C = \|\boldsymbol{r}_C\|$ being the Sun-chief distance) whose components in the rotating reference frame $\mathcal{T}_{R_C}$ are (see Fig. 1)

$$[\boldsymbol{r}_C]_{\mathcal{T}_{R_C}} = [R_C, \quad 0, \quad H_C]^{\mathrm{T}} \tag{2}$$

and R_C is the o-chief distance given by

$$R_C = \frac{a_C\,\left(1 - e_C^2\right)}{1 + e_C\,\cos f_C} \tag{3}$$

where a_C is the displaced orbit semimajor axis, and f_C is the chief true anomaly measured counterclockwise from the direction of the displaced orbit periapsis. Note that, since the chief is assumed to be synchronous with the planet, the components of the chief angular velocity $\boldsymbol{\omega}_C$ in frame $\mathcal{T}_{R_C}$ are

$$[\boldsymbol{\omega}_C]_{\mathcal{T}_R} = \left[0, \quad 0, \quad \dot{f}_C\right]^{\mathrm{T}} \tag{4}$$

with

$$\dot{f}_C = \frac{n_P\,\left(1 + e_C\,\cos f_C\right)^2}{\sqrt{\left(1 - e_C^2\right)^3}} \tag{5}$$

where $n_P \triangleq \sqrt{\mu_\odot / a_P^3}$ is the planet mean motion.

Taking into account the effect of RCD and using the approach of Ref. [24], the expression of the (chief) solar sail propulsive acceleration $\boldsymbol{a}_C$ can be written as

$$\boldsymbol{a}_C = \frac{\beta_C\,\mu_\odot}{2\,r_C^2}\,\left(\hat{\boldsymbol{r}}_C \cdot \hat{\boldsymbol{n}}_C\right)\,\left[u_C\,\hat{\boldsymbol{r}}_C + 2\,\left(1 - u_C\right)\,\left(\hat{\boldsymbol{r}}_C \cdot \hat{\boldsymbol{n}}_C\right)\,\hat{\boldsymbol{n}}_C\right] \tag{6}$$

where $\hat{\boldsymbol{r}}_C = \boldsymbol{r}_C / r_C$ is the Sun-chief unit vector, u_C is the chief reflectivity modulation ratio, β_C is the chief lightness number, defined as the ratio of the maximum propulsive acceleration modulus to the (local) solar gravitational acceleration ($\mu_\odot / r_C^2$), and $\hat{\boldsymbol{n}}_C$ is the sail normal unit vector in the direction opposite to the Sun. Note that the components of $\hat{\boldsymbol{n}}$ in frame $\mathcal{T}_{R_C}$ are

$$[\hat{\boldsymbol{n}}_C]_{\mathcal{T}_{R_C}} = [\cos\,(\alpha_C + \gamma_C)\,, \quad 0, \quad \sin\,(\alpha_C + \gamma_C)]^{\mathrm{T}} \tag{7}$$

where $\gamma_C \triangleq \arctan\left(H_C / R_C\right) \in [0,\, \pi/2]\,\mathrm{rad}$ is the elevation angle, that is, the angle between the Sun-chief line and plane $\mathcal{P}$, and $\alpha_C \triangleq \arccos\left(\hat{\boldsymbol{r}}_C \cdot \hat{\boldsymbol{n}}_C\right) \in [0,\, \pi/2]\,\mathrm{rad}$ is the sail cone angle. In particular, bearing in mind Eq. (3), the elevation angle can be written as a function of the displaced orbit characteristics $\{a_C, e_C \equiv e_P\}$ and the chief angular position f_C as

$$\gamma_C = \arctan\left(\frac{H_C\,\left(1 + e_C\,\cos f_C\right)}{a_C\,\left(1 - e_C^2\right)}\right) \tag{8}$$

On the other hand, the sail normal unit vector can be written as a function of the sail attitude as

$$[\hat{\boldsymbol{n}}_C]_{\mathcal{T}_{R_C}} = [\cos\theta_C\,\cos\varphi_C, \quad \sin\theta_C, \quad \cos\theta_C\,\sin\varphi_C]^{\mathrm{T}} \tag{9}$$

where θ_C is the angle between $\hat{\boldsymbol{n}}$ and the $(\hat{\boldsymbol{x}}_{R_C}, \hat{\boldsymbol{z}}_{R_C})$ plane, and φ_C is the angle measured from $\hat{\boldsymbol{x}}_{R_C}$ to the projection of $\hat{\boldsymbol{n}}_C$ onto the $(\hat{\boldsymbol{x}}_{R_C}, \hat{\boldsymbol{z}}_{R_C})$ plane, see Fig. 3. In particular, from Eqs. (7) and (9), the chief attitude angles are $\theta_C = 0$ and $\varphi_C = \alpha_C + \gamma_C$.

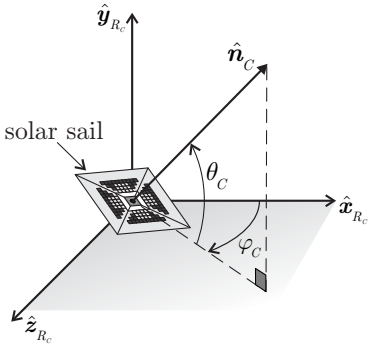

Figure 3: Attitude angles of the solar sail-based chief spacecraft.

According to Eq. (1), and taking into account Eqs. (2)–(7), the normal (i.e. along the $\hat{\boldsymbol{z}}_{R_C}$ direction) and radial (i.e. along the $\hat{\boldsymbol{x}}_{R_C}$ direction) components necessary to maintain a PFDO are

$$\frac{\mu_\odot}{r_C^2}\,\sin\gamma_C = \frac{\beta_C\,\mu_\odot}{2\,r_C^2}\,\cos\,\alpha_C\,\left[u_C\,\sin\,\gamma_C + 2\,\left(1-u_C\right)\,\cos\,\alpha_C\,\sin\,\left(\alpha_C+\gamma_C\right)\right] \tag{10}$$

$$\ddot{R}_C + \frac{\mu_\odot}{r_C^2}\,\cos\gamma_C - R_C\,\dot{f}_C^2 = \frac{\beta_C\,\mu_\odot}{2\,r_C^2}\,\cos\,\alpha_C\,\left[u_C\,\cos\,\gamma_C + 2\,\left(1-u_C\right)\,\cos\,\alpha_C\,\cos\,\left(\alpha_C+\gamma_C\right)\right] \tag{11}$$

After some algebraic manipulations (here omitted for the sake of brevity) on Eqs. (10)–(11), the value of the sail cone angle α_C required for maintaining a PFDO is found by solving the following sextic equation in the variable $\tan\alpha_C$

$$c_6\,\tan^6\alpha_C + c_5\,\tan^5\alpha_C + c_4\,\tan^4\alpha_C + c_3\,\tan^3\alpha_C + c_2\,\tan^2\alpha_C + c_1\,\tan\alpha_C + c_0 = 0 \tag{12}$$

where the coefficients $\{c_0, c_1, c_2, c_3, c_4, c_5, c_6\}$ are given by

$$c_6 = \frac{a_C^4\,H_C^2\,\left(1-e_C^2\,\cos^2\,f_C\right)^2}{a_P^6\,\left(1-e_C^2\right)^2} \tag{13}$$

$$c_5 = 4\,\left(a_C/a_P\right)^3\,\left[\frac{H_C\,\left(1-e_C^2\,\cos^2\,f_C\right)}{\sqrt{a_C^2\,\left(1-e_C^2\right)^2 + H_C^2\,\left(1+e_C\,\cos\,f_C\right)^2}} - \sqrt{c_6}\,\left(1-e_C\,\cos\,f_C\right)\right] \tag{14}$$

$$c_4 = 4\,\left[\frac{a_C\,\left(1-e_C^2\right)}{\sqrt{a_C^2\,\left(1-e_C^2\right)^2 + H_C^2\,\left(1+e_C\,\cos\,f_C\right)^2}} - \left(a_C/a_P\right)^3\,\left(1-e_C\,\cos\,f_C\right)\right]^2 - c_6 \tag{15}$$

$$c_3 = 0 \tag{16}$$

$$c_2 = c_4 - \frac{\beta_C^2\,a_C^2\,\left(1-e_C^2\right)^2}{a_C^2\,\left(1-e_C^2\right)^2 + H_C^2\,\left(1+e_C\,\cos\,f_C\right)^2} \tag{17}$$

$$c_1 = -c_5 \tag{18}$$

$$c_0 = c_6 \tag{19}$$

Those coefficients are function of the sail lightness number β_C, the chief angular position f_C, the planet orbit characteristics $\{a_P, e_P \equiv e_C\}$, and the displaced orbit characteristics $\{a_C, H_C\}$. The corresponding

value of the reflectivity modulation ratio u_C is given by

$$u_C = \frac{2\left[\sin\gamma_C - \beta_C\cos^2\alpha_C\sin\left(\alpha_C+\gamma_C\right)\right]}{\beta_C\cos\alpha_C\left[\sin\gamma_C - 2\cos\alpha_C\sin\left(\alpha_C+\gamma_C\right)\right]} \tag{20}$$

which is a function of β_C, the sail cone angle α_C, and the elevation angle γ_C. For illustrative purposes, consider now a chief spacecraft covering an Earth-synchronized elliptic PFDO with an eccentricity $e_C \equiv e_P = 0.0167$. In this scenario, Figs. 4-5 show the feasible regions with different constraints on the maximum value of the reflectivity modulation ratio $u_{C_{\max}}$, when the sail lightness number is $\beta_C = \{0.3,\, 0.6\}$. Note that the area of the feasible region enlarges as the values of $u_{C_{\max}}$ and β_C increase.

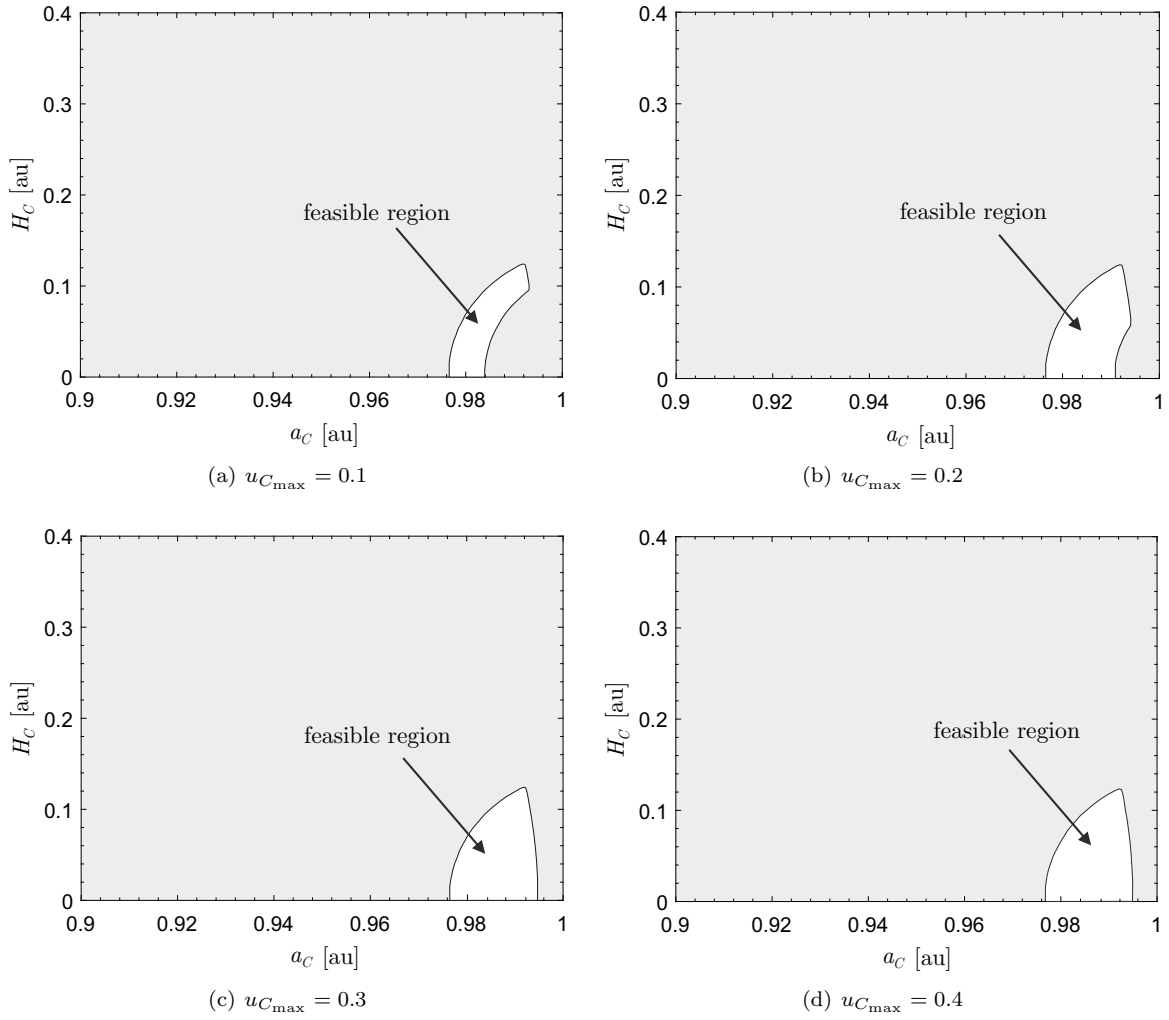

(a) $u_{C_{\max}} = 0.1$ (b) $u_{C_{\max}} = 0.2$

(c) $u_{C_{\max}} = 0.3$ (d) $u_{C_{\max}} = 0.4$

Figure 4: Feasible regions as a function of $\{a_C, H_C\}$ with $\beta_C = 0.3$ and $u_{C_{\max}} = \{0.1, 0.2, 0.3, 0.4\}$.

Consider, for example, an elliptic displaced orbit with a semimajor axis $a_C = 0.95\,\text{au}$ and a displacement $H_C = 0.05\,\text{au}$. Figure 6 shows that the cone angle α_C and the reflectivity modulation ratio u_C reach their maximum values when the chief is at the aphelion, whereas the minimum values are obtained at the perihelion of the displaced orbit.

2.2. Chief-deputy relative motion

Having analyzed the generation of an elliptic displaced orbit for the chief, we are now in a position to study the relative motion between chief and deputies. Taking into account Eq. (1), the equation of relative

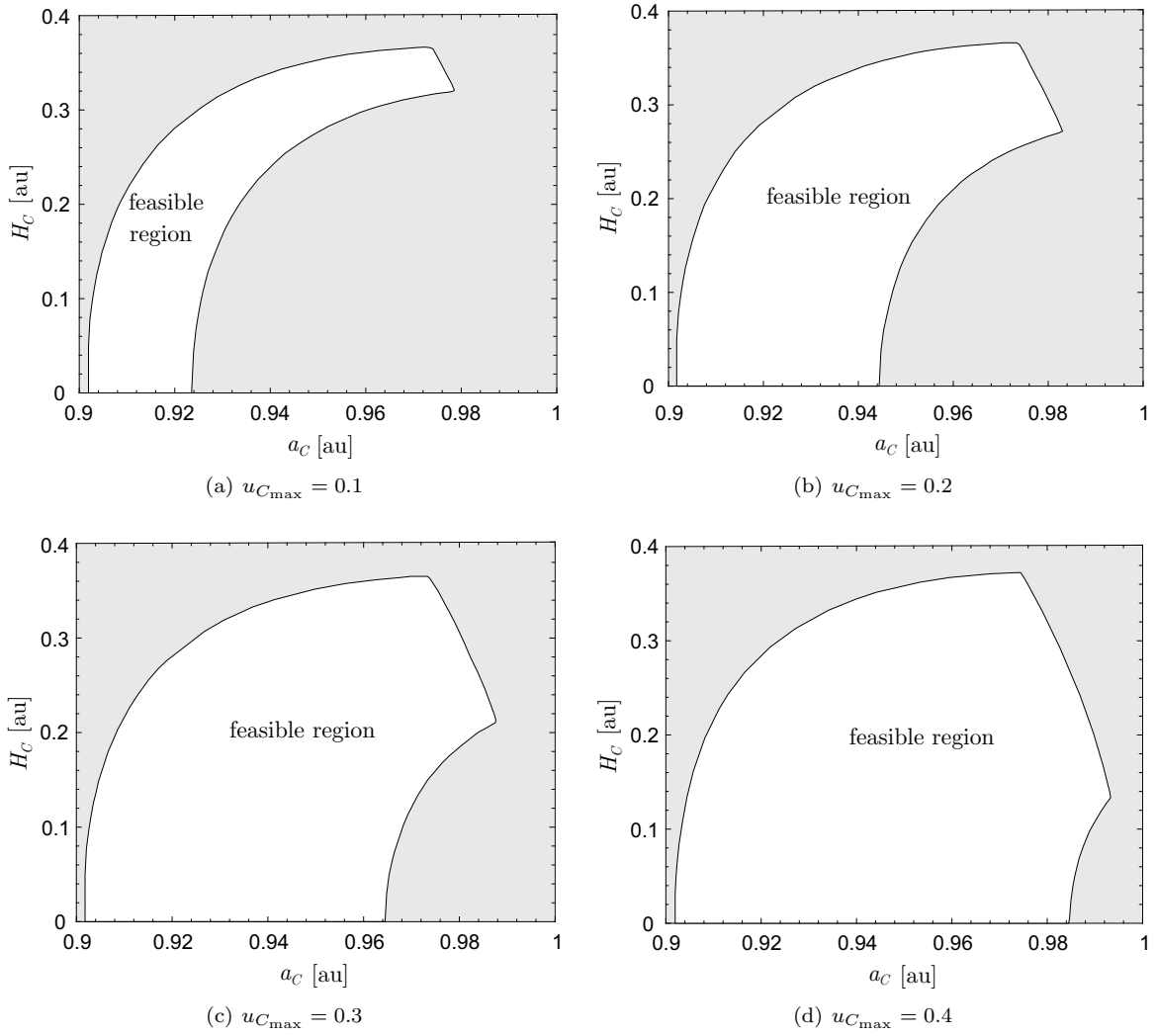

(a) $u_{C_{\max}} = 0.1$ (b) $u_{C_{\max}} = 0.2$

(c) $u_{C_{\max}} = 0.3$ (d) $u_{C_{\max}} = 0.4$

Figure 5: Feasible regions as a function of $\{a_C, H_C\}$ with $\beta_C = 0.6$ and $u_{C_{\max}} = \{0.1, 0.2, 0.3, 0.4\}$.

motion can be written as

$$\ddot{\boldsymbol{\rho}}_i + 2\,\boldsymbol{\omega}_C \times \dot{\boldsymbol{\rho}}_i + \dot{\boldsymbol{\omega}}_C \times \boldsymbol{\rho}_i + \boldsymbol{\omega}_C \times (\boldsymbol{\omega}_C \times \boldsymbol{\rho}_i) = -\frac{\mu_\odot}{r_i^3}\,\boldsymbol{r}_i + \frac{\mu_\odot}{r_C^3}\,\boldsymbol{r}_C + \boldsymbol{a}_i - \boldsymbol{a}_C \tag{21}$$

where $\boldsymbol{\rho}_i \triangleq \boldsymbol{r}_i - \boldsymbol{r}_C$ is the relative position vector between the i-th deputy and the chief spacecraft, see Fig. 7. Since the deputy sails operate in close vicinity of the chief, the relative distances among the solar sails are very small compared with the Sun-sail distance. Accordingly, paralleling the approach adopted in Ref. [16] and bearing in mind Eq. (6), the deputy propulsive and gravitational accelerations in Eq. (21) can be linearized around those of the chief as

$$\boldsymbol{a}_i \simeq \boldsymbol{a}_C + \frac{\partial \boldsymbol{a}_C}{\partial \boldsymbol{r}_C}\,\boldsymbol{\rho}_i + \frac{\partial \boldsymbol{a}_C}{\partial \hat{\boldsymbol{n}}_C}\,\Delta\hat{\boldsymbol{n}}_i + \frac{\partial \boldsymbol{a}_C}{\partial u_C}\,\Delta u_i \tag{22}$$

$$-\frac{\mu_\odot}{r_i^3}\,\boldsymbol{r}_i \simeq -\frac{\mu_\odot}{r_C^3}\,\boldsymbol{r}_C + \frac{\partial(-\mu_\odot\,\boldsymbol{r}_C/r_C^3)}{\partial \boldsymbol{r}_C}\,\boldsymbol{\rho}_i \tag{23}$$

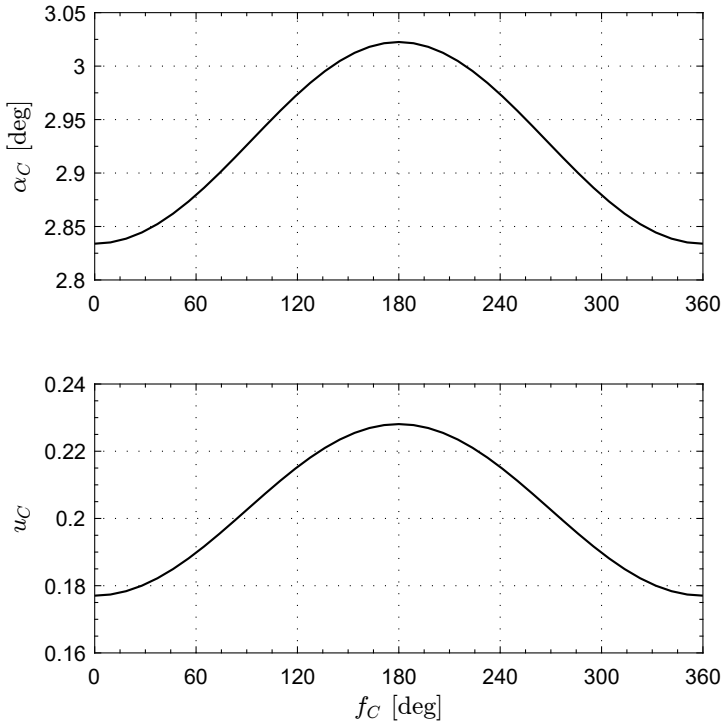

Figure 6: Cone angle and reflectivity modulation ratio of the chief spacecraft (with $\beta_C = 0.6$) during a single revolution.

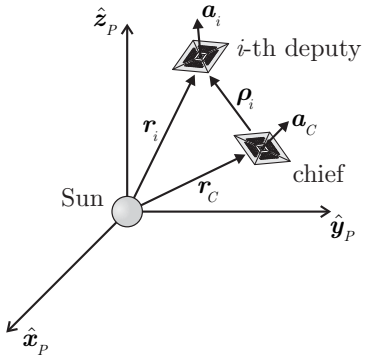

Figure 7: Relative position vector between the i-th deputy and the chief.

where $\Delta\,\hat{\boldsymbol{n}}_i \triangleq \hat{\boldsymbol{n}}_i - \hat{\boldsymbol{n}}_C$, and $\hat{\boldsymbol{n}}_i$ is the sail normal unit vector of the i-th deputy, $\Delta\,u_i \triangleq u_i - u_C$, and u_i is the reflectivity modulation ratio of the i-th deputy. Also

$$\frac{\partial \boldsymbol{a}_C}{\partial \boldsymbol{r}_C} = \frac{\beta_C\,\mu_\odot}{r_C^4}\left\{\frac{u_C}{2}\left[(\boldsymbol{r}_C\,\hat{\boldsymbol{n}}_C^{\mathrm{T}}) + (\hat{\boldsymbol{n}}_C\cdot\boldsymbol{r}_C)\,\mathbb{I}_3 - \frac{(\hat{\boldsymbol{n}}_C\cdot\boldsymbol{r}_C)\,(\boldsymbol{r}_C\,\boldsymbol{r}_C^{\mathrm{T}})}{r_C^2}\right]\right.$$
$$\left. + 2\,(1-u_C)\left[(\hat{\boldsymbol{n}}_C\cdot\boldsymbol{r}_C)\,(\hat{\boldsymbol{n}}_C\,\hat{\boldsymbol{n}}_C^{\mathrm{T}}) - \frac{2\,(\hat{\boldsymbol{n}}_C\cdot\boldsymbol{r}_C)^2\,(\hat{\boldsymbol{n}}_C\,\boldsymbol{r}_C^{\mathrm{T}})}{r_C^2}\right]\right\} \tag{24}$$

$$\frac{\partial \boldsymbol{a}_C}{\partial \hat{\boldsymbol{n}}_C} = \frac{\beta_C\,\mu_\odot}{r_C^4}\left\{\frac{u_C}{2}\,\boldsymbol{r}_C\,\boldsymbol{r}_C^{\mathrm{T}} + (1-u_C)\left[2\,(\hat{\boldsymbol{n}}_C\cdot\boldsymbol{r}_C)\,(\hat{\boldsymbol{n}}_C\,\boldsymbol{r}_C^{\mathrm{T}}) + (\hat{\boldsymbol{n}}_C\cdot\boldsymbol{r}_C)^2\,\mathbb{I}_3\right]\right\} \tag{25}$$

$$\frac{\partial \boldsymbol{a}_C}{\partial u_C} = \frac{\beta_C\,\mu_\odot}{r_C^4}\left[\frac{1}{2}\,(\hat{\boldsymbol{n}}_C\cdot\boldsymbol{r}_C)\,\boldsymbol{r}_C - (\hat{\boldsymbol{n}}_C\cdot\boldsymbol{r}_C)^2\,\hat{\boldsymbol{n}}_C\right] \tag{26}$$

$$\frac{\partial(-\mu_\odot\,\boldsymbol{r_C}/r_C^3)}{\partial \boldsymbol{r}_C} = \frac{3\,\mu_\odot}{r_C^5}\,\boldsymbol{r}_C\,\boldsymbol{r}_C^{\mathrm{T}} - \frac{\mu_\odot}{r_C^3}\,\mathbb{I}_3 \tag{27}$$

where $\mathbb{I}_3$ is the 3×3 identity matrix.

Bearing in mind that $\hat{\boldsymbol{n}}_i$ can be written in terms of φ_i and θ_i, see Eq. (9) and Fig. 3, it is possible to further linearize $\Delta\,\hat{\boldsymbol{n}}_i$ as

$$\Delta\hat{\boldsymbol{n}}_i \simeq \frac{\partial\hat{\boldsymbol{n}}_C}{\partial\,[\varphi_C,\ \theta_C]}\ [\Delta\,\varphi_i,\ \Delta\,\theta_i]^{\mathrm{T}} \tag{28}$$

where $\Delta\,\varphi_i \triangleq \varphi_i - \varphi_C$ and $\Delta\,\theta_i \triangleq \theta_i - \theta_C$ are the relative sail attitude angles, and the Jacobian matrix is given by

$$\frac{\partial\hat{\boldsymbol{n}}_C}{\partial\,[\varphi_C,\ \theta_C]} = \begin{bmatrix} -\sin\,\varphi_C\,\cos\,\theta_C & -\cos\,\varphi_C\,\sin\,\theta_C \\ 0 & \cos\,\theta_C \\ \cos\,\varphi_C\,\cos\,\theta_C & -\sin\,\varphi_C\,\sin\,\theta_C \end{bmatrix} \tag{29}$$

Substituting Eqs. (22)–(29) into Eq. (21), the linear differential equation of the relative motion between the i-th deputy and the chief is

$$\ddot{\boldsymbol{\rho}}_i + 2\,\mathbb{M}_v\,\dot{\boldsymbol{\rho}}_i + \mathbb{M}_p\,\boldsymbol{\rho}_i = \mathbb{M}_c\,\boldsymbol{u}_i \tag{30}$$

where $\boldsymbol{u}_i$ is the control input of the i-th deputy, given by

$$\boldsymbol{u}_i = [\Delta\,\varphi_i,\ \Delta\,\theta_i,\ \Delta\,u_i]^{\mathrm{T}} \tag{31}$$

whereas $\mathbb{M}_v$, $\mathbb{M}_p$, and $\mathbb{M}_c$ are the coefficient matrices defined as

$$\mathbb{M}_v \triangleq \begin{bmatrix} 0 & -\omega_C & 0 \\ \omega_C & 0 & 0 \\ 0 & 0 & 0 \end{bmatrix} \tag{32}$$

$$\mathbb{M}_p \triangleq \dot{\mathbb{M}}_v - \mathrm{diag}\left(\omega_C^2,\ \omega_C^2,\ 0\right) - \frac{\partial\boldsymbol{a}_C}{\partial\boldsymbol{r}_C} - \frac{\partial(-\mu_\odot\,\boldsymbol{r}_C/r_C^3)}{\partial\boldsymbol{r}_C} \tag{33}$$

$$\mathbb{M}_c \triangleq \left[\frac{\partial\,\boldsymbol{a}_C}{\partial\,\hat{\boldsymbol{n}}_C}\,\frac{\partial\,\hat{\boldsymbol{n}}_C}{\partial\,[\varphi_C,\theta_C]},\quad \frac{\partial\,\boldsymbol{a}_C}{\partial u_C}\right] \tag{34}$$

Note that, from Eqs. (25)–(26), it can be verified that the matrix $\mathbb{M}_c$ in Eq. (34) is nonsingular provided $\beta_C \neq 0$.

In the following analysis, the relative trajectory tracking problem involving the formation system described by Eq. (30) will be addressed. In particular, distributed cooperative control strategies are presented for two important cases: 1) with full state feedback; 2) without relative velocity measurement. In both cases the formation maintenance error eventually approaches zero while consensus is preserved during transition.

3. Solar sail formation flying via consensus control

The consensus control algorithms are now developed for a spacecraft formation architecture with a single chief and $N \geq 2$ deputies, based on a local neighbor-to-neighbor information exchange. In particular, the communication topology of the relative motion is described by an undirected graph, under the assumption that the information exchange is bidirectional.

A few pertinent concepts of graph theory are first reviewed, according to Ref. [29]. A weighted undirected graph $\mathcal{G}$ consists of a finite non-empty vertex set $\mathcal{V} \triangleq \{\upsilon_1, \ldots, \upsilon_N\}$, an edge set $\mathcal{E} \triangleq \{(\upsilon_1, \upsilon_2), \ldots, (\upsilon_{N-1}, \upsilon_N)\} \subseteq \mathcal{V} \times \mathcal{V}$, and a weighted adjacency matrix $\mathbb{W} = [w_{ij}] \in \mathbb{R}^{N\times N}$. The matrix $\mathbb{W}$ is defined such that its generic entry $w_{ij} = w_{ij} \in \mathbb{R}^+$ if $(\upsilon_i, \upsilon_j) \in \mathcal{E}$ with $i \neq j$, whereas $w_{ii} = 0$. Note that the matric $\mathbb{W}$ is symmetric, and $w_{ij} = 0$ if $(\upsilon_i, \upsilon_j) \notin \mathcal{E}$. The Laplacian matrix $\mathbb{L} = [l_{ij}] \in \mathbb{R}^{N\times N}$ associated with $\mathbb{W}$ is defined as $l_{ij} = -w_{ij}$ and $l_{ii} = \sum_{j=1}^{N} w_{ij}, \forall\, i \neq j$. In addition, the matrix $\mathbb{L}$ is symmetric positive semi-definite, and $\sum_{j=1}^{N} l_{ij} = 0, \forall\, i \neq j$. Finally, an undirected graph is called connected if there exists a path from every vertex to every other vertex.

In the following discussion, emphasis is focused on the cases where the information exchange topology is fixed and the weights w_{ij} are constant. In modeling the topology of the solar sail-based formation architecture during the relative motion, each deputy spacecraft is represented by a vertex, while the data flow between any two deputies is characterized by a weighted edge. In particular, assume that each deputy has access to the state information of the chief, that is, the topology graph $\mathcal{G}$ is connected.

3.1. Consensus control with full state feedback

Consider first the case where the consensus protocol is formulated via full state feedback, that is, both the relative position and relative velocity information are available when there is a path between two deputies (i.e., two vertices). Let $(\boldsymbol{\rho}_i^\star, \dot{\boldsymbol{\rho}}_i^\star) \in \mathbb{R}^3 \times \mathbb{R}^3$ denote the desired relative trajectory of the i-th deputy with respect to the chief, and introduce the position error $\boldsymbol{e}_i \triangleq \boldsymbol{\rho}_i - \boldsymbol{\rho}_i^\star$ and the velocity error $\dot{\boldsymbol{e}}_i \triangleq \dot{\boldsymbol{\rho}}_i - \dot{\boldsymbol{\rho}}_i^\star$. The aim of the developed controller is to drive each deputy towards the desired relative trajectory, viz. $\boldsymbol{e}_i \to \mathbf{0}$ and $\dot{\boldsymbol{e}}_i \to \mathbf{0}$, while consensus (i.e. $\boldsymbol{e}_i \to \boldsymbol{e}_j$ and $\dot{\boldsymbol{e}}_i \to \dot{\boldsymbol{e}}_j$) is guaranteed during the transition phase by exploiting the available information data transmitted from the local neighbors. To this end, the cooperative control law for the system represented by Eq. (30) is designed as [30]

$$\boldsymbol{u}_i = \mathbb{M}_c^{-1} \left\{ \ddot{\boldsymbol{\rho}}_i^\star + 2\,\mathbb{M}_v\,\dot{\boldsymbol{\rho}}_i^\star + \mathbb{M}_p\,\boldsymbol{\rho}_i - \lambda_i^p\,\boldsymbol{e}_i - \lambda_i^v\,\dot{\boldsymbol{e}}_i - \sum_{j=1}^{N} w_{ij}^p\,(\boldsymbol{e}_i - \boldsymbol{e}_j) - \sum_{j=1}^{N} w_{ij}^v\,(\dot{\boldsymbol{e}}_i - \dot{\boldsymbol{e}}_j) \right\} \tag{35}$$

where $\{\lambda_i^p, \lambda_i^v\} \in \mathbb{R}^+$, w_{ij}^p and w_{ij}^v are the (i,j) entries of the weighted adjacency matrices $\mathbb{W}_p$ and $\mathbb{W}_v$, respectively. Note that $\mathbb{W}_p$ and $\mathbb{W}_v$ are allowed to be different and, in particular, the last two terms in Eq. (35) are designed to maintain the formation during the transition phase, while the other terms are selected in order to drive each deputy towards the desired relative trajectory.

Theorem 1: Using the control law given by Eq. (35) for the system represented by Eq. (30), consensus tracking is asymptotically achieved, that is, $\boldsymbol{e}_i \to \boldsymbol{e}_j \to \mathbf{0}$ and $\dot{\boldsymbol{e}}_i \to \dot{\boldsymbol{e}}_j \to \mathbf{0}$ as $t \to \infty$.

Proof: Consider the candidate Lyapunov function V defined as

$$V \triangleq \frac{1}{2} \sum_{i=1}^{N} \lambda_i^p\,\boldsymbol{e}_i^{\mathrm{T}}\,\boldsymbol{e}_i + \frac{1}{2} \sum_{i=1}^{N} \dot{\boldsymbol{e}}_i^{\mathrm{T}}\,\dot{\boldsymbol{e}}_i + \frac{1}{4} \sum_{i=1}^{N} \sum_{j=1}^{N} w_{ij}^p\,(\boldsymbol{e}_i - \boldsymbol{e}_j)^{\mathrm{T}}\,(\boldsymbol{e}_i - \boldsymbol{e}_j) \tag{36}$$

Note that V is positive definite, and its time derivative is given by

$$\dot{V} = \sum_{i=1}^{N} \lambda_i^p\,\boldsymbol{e}_i^{\mathrm{T}}\,\dot{\boldsymbol{e}}_i + \sum_{i=1}^{N} \dot{\boldsymbol{e}}_i^{\mathrm{T}} \left[-2\,\mathbb{M}_v\,\dot{\boldsymbol{e}}_i - \lambda_i^p\,\boldsymbol{e}_i - \lambda_i^v\,\dot{\boldsymbol{e}}_i - \sum_{j=1}^{N} w_{ij}^p\,(\boldsymbol{e}_i - \boldsymbol{e}_j) - \sum_{j=1}^{N} w_{ij}^v\,(\dot{\boldsymbol{e}}_i - \dot{\boldsymbol{e}}_j) \right] +$$

$$+ \frac{1}{2} \sum_{i=1}^{N} \sum_{j=1}^{N} w_{ij}^p\,(\boldsymbol{e}_i - \boldsymbol{e}_j)^{\mathrm{T}}\,(\dot{\boldsymbol{e}}_i - \dot{\boldsymbol{e}}_j) \tag{37}$$

Bearing in mind Eq. (32), the matrix $\mathbb{M}_v$ is skew symmetric and, therefore, $\dot{\boldsymbol{e}}_i^{\mathrm{T}}\,\mathbb{M}_v\,\dot{\boldsymbol{e}}_i = 0$. Recalling that $w_{ij}^p = w_{ji}^p$, the following relationship holds

$$\sum_{i=1}^{N} \sum_{j=1}^{N} \dot{\boldsymbol{e}}_i^{\mathrm{T}}\,w_{ij}^p\,(\boldsymbol{e}_i - \boldsymbol{e}_j) = \frac{1}{2} \sum_{i=1}^{N} \sum_{j=1}^{N} \dot{\boldsymbol{e}}_i^{\mathrm{T}}\,w_{ij}^p\,(\boldsymbol{e}_i - \boldsymbol{e}_j) + \frac{1}{2} \sum_{j=1}^{N} \sum_{i=1}^{N} \dot{\boldsymbol{e}}_j^{\mathrm{T}}\,w_{ji}^p\,(\boldsymbol{e}_j - \boldsymbol{e}_i) =$$

$$= \frac{1}{2} \sum_{i=1}^{N} \sum_{j=1}^{N} w_{ij}^p\,(\dot{\boldsymbol{e}}_i - \dot{\boldsymbol{e}}_j)^{\mathrm{T}}\,(\boldsymbol{e}_i - \boldsymbol{e}_j) \tag{38}$$

so that

$$\sum_{i=1}^{N} \sum_{j=1}^{N} \dot{\boldsymbol{e}}_i^{\mathrm{T}}\,w_{ij}^v\,(\dot{\boldsymbol{e}}_i - \dot{\boldsymbol{e}}_j) = \frac{1}{2} \sum_{i=1}^{N} \sum_{j=1}^{N} w_{ij}^v\,(\dot{\boldsymbol{e}}_i - \dot{\boldsymbol{e}}_j)^{\mathrm{T}}\,(\dot{\boldsymbol{e}}_i - \dot{\boldsymbol{e}}_j) \tag{39}$$

Substituting Eqs. (38)–(39) into Eq. (37), the time derivative of the Lyapunov function becomes

$$\dot{V} = -\sum_{i=1}^{N} \lambda_i^v \, \dot{\boldsymbol{e}}_i^{\mathrm{T}} \, \dot{\boldsymbol{e}}_i - \frac{1}{2} \sum_{i=1}^{N} \sum_{j=1}^{N} w_{ij}^v \, (\dot{\boldsymbol{e}}_i - \dot{\boldsymbol{e}}_j)^{\mathrm{T}} \, (\dot{\boldsymbol{e}}_i - \dot{\boldsymbol{e}}_j) \leq 0 \tag{40}$$

Note that the formation system described by Eq. (30) is non-autonomous, since its coefficients are time dependent. Therefore, Matrosov's theorem [31] is here adopted for convergence analysis. To that end, let

$$F \, (\boldsymbol{e}_i, \dot{\boldsymbol{e}}_i) \triangleq \sum_{i=1}^{N} \boldsymbol{e}_i^{\mathrm{T}} \, \dot{\boldsymbol{e}}_i \tag{41}$$

Since $\dot{V}$ is semi-negative definite, see Eq. (40), it follows that $\{\boldsymbol{e}_i, \dot{\boldsymbol{e}}_i\}$ is uniformly bounded and so is the function F. Also, $\dot{V} = 0$ implies $\dot{\boldsymbol{e}}_i = \boldsymbol{0}$, therefore the time derivative of F on domain $\mathcal{D} \triangleq \left\{ (\boldsymbol{e}_i, \dot{\boldsymbol{e}}_i) \,|\, \dot{V} = 0 \right\} = \{ (\boldsymbol{e}_i, \dot{\boldsymbol{e}}_i) \,|\, \dot{\boldsymbol{e}}_i = \boldsymbol{0} \}$ can be written as

$$\dot{F} = -\sum_{i=1}^{N} \lambda_i^p \, \boldsymbol{e}_i^{\mathrm{T}} \, \boldsymbol{e}_i - \sum_{i=1}^{N} \sum_{j=1}^{N} w_{ij}^p \, \boldsymbol{e}_i^{\mathrm{T}} \, (\boldsymbol{e}_i - \boldsymbol{e}_j) = -\sum_{i=1}^{N} \lambda_i^p \, \boldsymbol{e}_i^{\mathrm{T}} \, \boldsymbol{e}_i - \frac{1}{2} \sum_{i=1}^{N} \sum_{j=1}^{N} w_{ij}^p \, (\boldsymbol{e}_i - \boldsymbol{e}_j)^{\mathrm{T}} \, (\boldsymbol{e}_i - \boldsymbol{e}_j) \leq 0 \tag{42}$$

Note that $|\dot{F}|$ is positive definite for any $\boldsymbol{e}_i \neq \boldsymbol{0}$. As a result, there exists a class $\mathcal{K}$ function $\Re$, such that $|\dot{F}| \geq \Re \left(\|\boldsymbol{e}_i\| \right)$. According to Matrosov's theorem, the equilibrium of the system under the control law Eq. (35) is uniformly asymptotically stable, that is, $\boldsymbol{e}_i \to \boldsymbol{e}_j \to \boldsymbol{0}$ and $\dot{\boldsymbol{e}}_i \to \dot{\boldsymbol{e}}_j \to \boldsymbol{0}$ as $t \to \infty$. This complete the proof.

3.2. Consensus without relative velocity measurement

The distributed control law given by Eq. (35) requires each deputy to know the relative velocities of its local neighbors. However, in many cases of practical interest such an information is not available, especially for solar sail-based spacecraft with a small payload and instrument mass. Moreover, even when the spacecraft is equipped with a (relative) velocity sensor, the precision still remains questionable for large baseline formation missions. These two issues require finding an alternative algorithm accounting for the unavailability of relative velocity measurement. To this end, the consensus strategy is proposed as [32]

$$\dot{\boldsymbol{\xi}}_i = \boldsymbol{\Phi} \, \boldsymbol{\xi}_i + \lambda_i^v \, \boldsymbol{e}_i + \sum_{j=1}^{N} w_{ij}^v \, (\boldsymbol{e}_i - \boldsymbol{e}_j) \tag{43}$$

$$\boldsymbol{\zeta}_i = \boldsymbol{\Gamma} \left[\boldsymbol{\Phi} \, \boldsymbol{\xi}_i + \lambda_i^v \, \boldsymbol{e}_i + \sum_{j=1}^{N} w_{ij}^v \, (\boldsymbol{e}_i - \boldsymbol{e}_j) \right] \tag{44}$$

$$\boldsymbol{u}_i = \mathbb{M}_c^{-1} \left\{ \ddot{\boldsymbol{\rho}}_i^{\star} + 2 \, \mathbb{M}_v \, \dot{\boldsymbol{\rho}}_i^{\star} + \mathbb{M}_p \, \boldsymbol{\rho}_i - \lambda_i^p \, \boldsymbol{e}_i - \sum_{j=1}^{N} w_{ij}^p \, (\boldsymbol{e}_i - \boldsymbol{e}_j) - \boldsymbol{\zeta}_i \right\} \tag{45}$$

where $\{\boldsymbol{\xi}_i, \boldsymbol{\zeta}_i\} \in \mathbb{R}^3$, $\{\lambda_i^p, \ \lambda_i^v, \ w_{ij}^p, \ w_{ij}^v\}$ are defined as in Eq. (35), the matrix $\boldsymbol{\Phi} \in \mathbb{R}^{3 \times 3}$ is Hurwitz, and $\boldsymbol{\Gamma} = \boldsymbol{\Gamma}^{\mathrm{T}} \in \mathbb{R}^{3 \times 3}$ is the positive-definite solution to the Lyapunov equation $\boldsymbol{\Phi}^{\mathrm{T}} \, \boldsymbol{\Gamma} + \boldsymbol{\Gamma} \, \boldsymbol{\Phi} = -\boldsymbol{\Theta}$ where $\boldsymbol{\Theta} = \boldsymbol{\Theta}^{\mathrm{T}} \in \mathbb{R}^{3 \times 3}$ is positive-definite. In particular, since no relative velocity information is used, w_{ij}^v can be thought of playing a similar role as in Eq. (35). Note that the terms involving the relative velocity requirement in Eq. (35) are now replaced by the output of a passive filter, as is shown in Eqs. (43)–(44).

Theorem 2: Using the control law given by Eq. (45) for the system represented by Eq. (30), consensus is asymptotically reached, that is, $\boldsymbol{e}_i \to \boldsymbol{e}_j \to \boldsymbol{0}$ and $\dot{\boldsymbol{e}}_i \to \dot{\boldsymbol{e}}_j \to \boldsymbol{0}$ as $t \to \infty$.

Proof: Consider the candidate Lyapunov function V defined as

$$V \triangleq \frac{1}{2} \sum_{i=1}^{N} \lambda_i^p \, \boldsymbol{e}_i^{\mathrm{T}} \, \boldsymbol{e}_i + \frac{1}{2} \sum_{i=1}^{N} \dot{\boldsymbol{e}}_i^{\mathrm{T}} \, \dot{\boldsymbol{e}}_i + \frac{1}{4} \sum_{i=1}^{N} \sum_{j=1}^{N} w_{ij}^p \, (\boldsymbol{e}_i - \boldsymbol{e}_j)^{\mathrm{T}} \, (\boldsymbol{e}_i - \boldsymbol{e}_j) + \frac{1}{2} \, \dot{\boldsymbol{\xi}}^{\mathrm{T}} \, \left(\bar{\mathbb{L}}_v \otimes \mathbb{I}_3 \right)^{-1} \, (\mathbb{I}_N \otimes \boldsymbol{\Gamma}) \, \dot{\boldsymbol{\xi}} \tag{46}$$

where $\otimes$ denotes the Kronecker product, $\boldsymbol{\xi} \triangleq [\boldsymbol{\xi}_1^{\mathrm{T}}, \ldots, \boldsymbol{\xi}_N^{\mathrm{T}}]^{\mathrm{T}}$, $\bar{\mathbb{L}}_v \triangleq \mathbb{L}_v + \mathrm{diag}\,(\lambda_1^v,\ \ldots,\ \lambda_N^v)$. Since the Laplacian matrix $\mathbb{L}_v = \left[l_{ij}^v\right] \in \mathbb{R}^{N\times N}$ associated with $\mathbb{W}_v = \left[w_{ij}^v\right] \in \mathbb{R}^{N\times N}$ is symmetric positive semi-definite, it follows that $\bar{\mathbb{L}}_v$ is symmetric positive definite, and so is $\bar{\mathbb{L}}_v^{-1}$. The time derivative of V can be written as

$$\dot{V} = \sum_{i=1}^{N} \lambda_i^p\, \boldsymbol{e}_i^{\mathrm{T}}\, \dot{\boldsymbol{e}}_i + \sum_{i=1}^{N} \dot{\boldsymbol{e}}_i^{\mathrm{T}} \left[-2\,\mathbb{M}_v\, \dot{\boldsymbol{e}}_i - \lambda_i^p\, \boldsymbol{e}_i - \sum_{j=1}^{N} w_{ij}^p\, (\boldsymbol{e}_i - \boldsymbol{e}_j) - \boldsymbol{\zeta}_i\right] +$$

$$+ \frac{1}{2} \sum_{i=1}^{N}\sum_{j=1}^{N} w_{ij}^p\, (\boldsymbol{e}_i - \boldsymbol{e}_j)^{\mathrm{T}}\, (\dot{\boldsymbol{e}}_i - \dot{\boldsymbol{e}}_j) + \frac{1}{2}\, \ddot{\boldsymbol{\xi}}^{\mathrm{T}}\, \left(\bar{\mathbb{L}}_v \otimes \mathbb{I}_3\right)^{-1}\, (\mathbb{I}_N \otimes \boldsymbol{\Gamma})\, \dot{\boldsymbol{\xi}} + \frac{1}{2}\, \dot{\boldsymbol{\xi}}^{\mathrm{T}}\, \left(\bar{\mathbb{L}}_v \otimes \mathbb{I}_3\right)^{-1}\, (\mathbb{I}_N \otimes \boldsymbol{\Gamma})\, \ddot{\boldsymbol{\xi}} \quad (47)$$

After some mathematical manipulations, Eq. (47) reduces to

$$\dot{V} = -\frac{1}{2}\, \dot{\boldsymbol{\xi}}^{\mathrm{T}}\, \left(\bar{\mathbb{L}}_v^{-1} \otimes \boldsymbol{\Theta}\right)\, \dot{\boldsymbol{\xi}} \leq 0 \quad (48)$$

Since the time derivative $\dot{V}$ given by Eq. (48) is a function of $\dot{\boldsymbol{\xi}}_i$ rather than $\dot{\boldsymbol{e}}_i$, Matrosov's theorem cannot be directly applied. Instead, the Barbalat's lemma [33] is here used for convergence analysis. In Eq. (46), V is a positive definite function of $\left\{\boldsymbol{e}_i,\ \dot{\boldsymbol{e}}_i,\ \boldsymbol{e}_i - \boldsymbol{e}_j,\ \dot{\boldsymbol{\xi}}\right\}$, and Eq. (48) implies $\dot{V} \leq 0$, therefore $\{\boldsymbol{e}_i,\ \dot{\boldsymbol{e}}_i,\ \boldsymbol{e}_i - \boldsymbol{e}_j,\ \dot{\boldsymbol{\xi}}\}$ are all bounded. Since $\boldsymbol{\Phi}$ is Hurwitz, it can be drawn from Eq. (43) that $\ddot{\boldsymbol{\xi}}$ is bounded, from which

$$\left|\ddot{V}\right| = \frac{1}{2}\, \left|\ddot{\boldsymbol{\xi}}^{\mathrm{T}}\, \left(\bar{\mathbb{L}}_v^{-1} \otimes \boldsymbol{\Theta}\right)\, \dot{\boldsymbol{\xi}} + \dot{\boldsymbol{\xi}}^{\mathrm{T}}\, \left(\bar{\mathbb{L}}_v^{-1} \otimes \boldsymbol{\Theta}\right)\, \ddot{\boldsymbol{\xi}}\right| \leq \left\|\left(\bar{\mathbb{L}}_v^{-1} \otimes \boldsymbol{\Theta}\right)\, \dot{\boldsymbol{\xi}}\right\|\, \left\|\ddot{\boldsymbol{\xi}}\right\| \quad (49)$$

Equation (49) shows that $\ddot{V}$ is also bounded, and hence $\dot{V}$ is uniformly continuous. According to the Barbalat's lemma, $\dot{V} \to 0$ as $t \to \infty$, which further results in $\dot{\boldsymbol{\xi}} \to \boldsymbol{0}$. From Eq. (43) $\dddot{\boldsymbol{\xi}}$ is bounded, therefore $\ddot{\boldsymbol{\xi}}$ is uniformly continuous. Using the Barbalat's lemma, $\ddot{\boldsymbol{\xi}} \to \boldsymbol{0}$ as $t \to \infty$. For the sake of convenience, Eq. (43) may be rearranged into a compact form as

$$\dot{\boldsymbol{\xi}} = (\mathbb{I}_N \otimes \boldsymbol{\Phi})\, \boldsymbol{\xi} + \left(\bar{\mathbb{L}}_v \otimes \mathbb{I}_3\right)\, \boldsymbol{e} \quad (50)$$

where $\boldsymbol{e} \triangleq [\boldsymbol{e}_1^{\mathrm{T}}, \ldots, \boldsymbol{e}_N^{\mathrm{T}}]^{\mathrm{T}}$. Recalling that $\left\{\dot{\boldsymbol{\xi}},\ \ddot{\boldsymbol{\xi}}\right\} \to \boldsymbol{0}$, Eq. (50) states that $\dot{\boldsymbol{e}} \to \boldsymbol{0}$. Likewise, it can be verified that $\ddot{\boldsymbol{e}} \to \boldsymbol{0}$. Using the control law given by Eq. (45), the error equation of the formation system described by Eq. (30) becomes

$$\ddot{\boldsymbol{e}} + 2\, (\mathbb{I}_N \otimes \mathbb{M}_v)\, \dot{\boldsymbol{e}} + \left(\bar{\mathbb{L}}_p \otimes \mathbb{I}_3\right)\, \boldsymbol{e} + (\mathbb{I}_N \otimes \boldsymbol{\Gamma})\, \dot{\boldsymbol{\xi}} = \boldsymbol{0} \quad (51)$$

Since $\left\{\dot{\boldsymbol{e}},\ \ddot{\boldsymbol{e}},\ \dot{\boldsymbol{\xi}}\right\} \to \boldsymbol{0}$, therefore $\left(\bar{\mathbb{L}}_p \otimes \mathbb{I}_3\right)\, \boldsymbol{e} = \boldsymbol{0}$, which amounts to stating that $\boldsymbol{e} \to \boldsymbol{0}$. This complete the proof.

4. Numerical simulations

To illustrate the performance of the developed consensus-based control law, a formation mission scenario is now discussed, with a chief spacecraft (S_C) and three surrounding deputies (S_i with $i = \{1,\ 2,\ 3\}$) that are coordinated through local communication. The chief covers an Earth-synchronized PFDO (i.e. $e_C = 0.0167$) with semimajor axis $a_C = 0.95\,\mathrm{au}$, and displacement $H_C = 0.05\,\mathrm{au}$, while all deputies are driven towards the prescribed trajectory with different phases. In the chief rotating reference frame $\mathcal{T}_{R_C}$, the parametric solution of the i-th deputy trajectory (relative to the chief) is assumed to have the following algebraic form

$$\boldsymbol{\rho}_i^{\star} = \left[100\, \sin\,(n_r\, t + \phi_i)\,,\quad 200\, \cos\,(n_r\, t + \phi_i)\,,\quad 100\,\sqrt{3}\, \sin\,(n_r\, t + \phi_i)\right]^{\mathrm{T}}\ \mathrm{km} \quad (52)$$

where $n_r \triangleq 100\, n_P$ is the angular velocity of the relative orbit, and $\phi_i = 2\,(i-1)\,\pi/3$ is the phase angle.

4.1. Case A: full relative state information is available

Consider first the case where a full relative state information is available when a path between two deputies exists. The corresponding communication topology graph of the formation system is shown in Fig. 8, whereas the position ($\mathbb{W}_p$) and velocity ($\mathbb{W}_v$) weighted adjacency matrices among deputies are given by

$$\mathbb{W}_p = \begin{bmatrix} 0 & 1 & 2 \\ 1 & 0 & 0 \\ 2 & 0 & 0 \end{bmatrix} \quad , \quad \mathbb{W}_v = \begin{bmatrix} 0 & 5\times10^{-3} & 1\times10^{-2} \\ 5\times10^{-3} & 0 & 0 \\ 1\times10^{-2} & 0 & 0 \end{bmatrix} \tag{53}$$

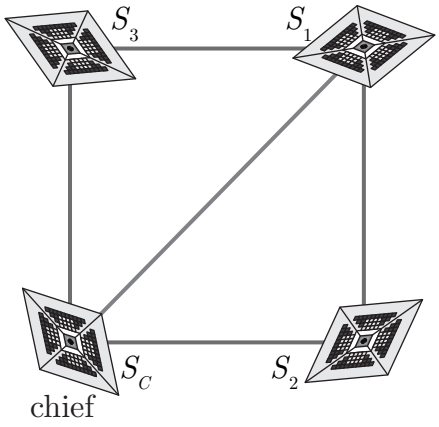

Figure 8: Information exchange topology among the solar sail formation system.

The initial conditions of the three deputies are assumed slightly different from the desired trajectories, and the initial errors $\boldsymbol{e}_0 \triangleq [e_{x_0}, e_{y_0}, e_{z_0}]^{\mathrm{T}}$ are reported in Tab. 1. Using a trial and error procedure, a satisfactory control performance (in terms of convergence time and tracking accuracy) is obtained when the dimensionless parameters are selected as $\lambda_i^p = 5\times10^3$ and $\lambda_i^v = 25$. Accordingly, the position and velocity

	e_{x_0} [km]	e_{y_0} [km]	e_{z_0} [km]	$\dot{e}_{x_0}$ [m/s]	$\dot{e}_{y_0}$ [m/s]	$\dot{e}_{z_0}$ [m/s]
S_1	40	−20	20	1×10^{-5}	-2×10^{-5}	3×10^{-5}
S_2	−20	20	−40	-2×10^{-5}	1×10^{-5}	-1×10^{-5}
S_3	−40	−20	40	2×10^{-5}	-1×10^{-5}	-3×10^{-5}

Table 1: Initial errors of three deputies in the full state feedback case.

errors of the three deputies are drawn in Fig. 9 and Fig. 10 respectively, while the variations of control inputs $\Delta\varphi_i$, $\Delta\theta_i$, and Δu_i are shown in Fig. 11. Figure 12 illustrates the actual position of the three deputies (denoted with a circle, a square and a star) when compared with the desired position (denoted with a dot). These positions are calculated at $t = \{0,\ 5,\ 10,\ 15\}$ days and are projected on the $(\hat{\boldsymbol{x}}_{R_C}, \hat{\boldsymbol{y}}_{R_C})$ plane. Note that Fig. 12 shows how the control law given by Eq. (35) allows the three deputies to be perfectly synchronized with negligible final errors.

4.2. Case B: The relative velocity information is unavailable

In this case, the initial errors are assumed to take the same value as those listed in Tab. 1, and the position and velocity weighted adjacency matrices are given by

$$\mathbb{W}_p = \begin{bmatrix} 0 & 1 & 2 \\ 1 & 0 & 0 \\ 2 & 0 & 0 \end{bmatrix} \quad , \quad \mathbb{W}_v = \begin{bmatrix} 0 & 500 & 1000 \\ 500 & 0 & 0 \\ 1000 & 0 & 0 \end{bmatrix} \tag{54}$$

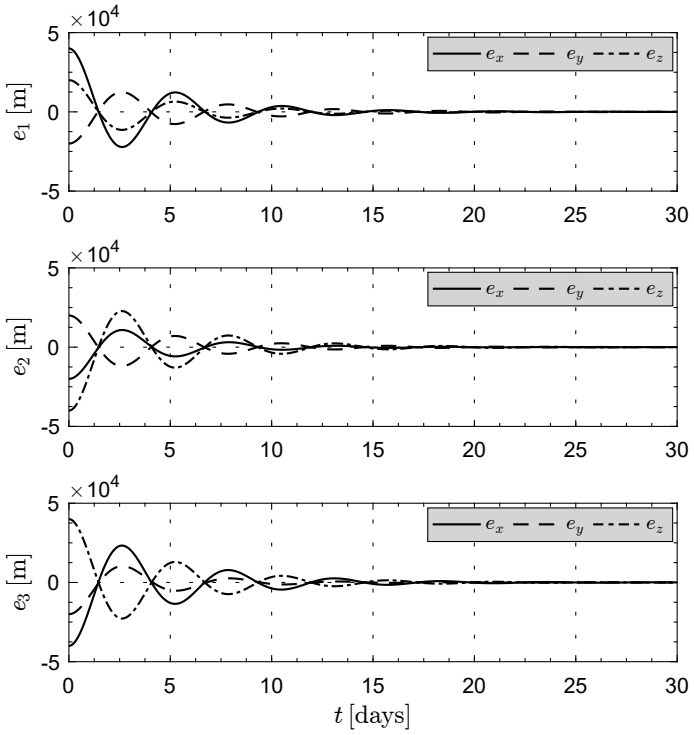

Figure 9: Components of the position error in the full state feedback case.

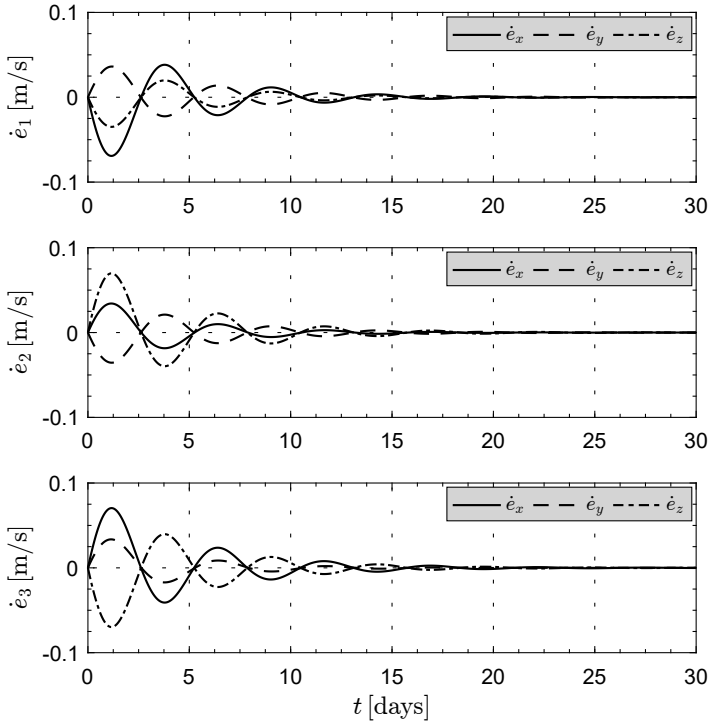

Figure 10: Components of the velocity error in the full state feedback case.

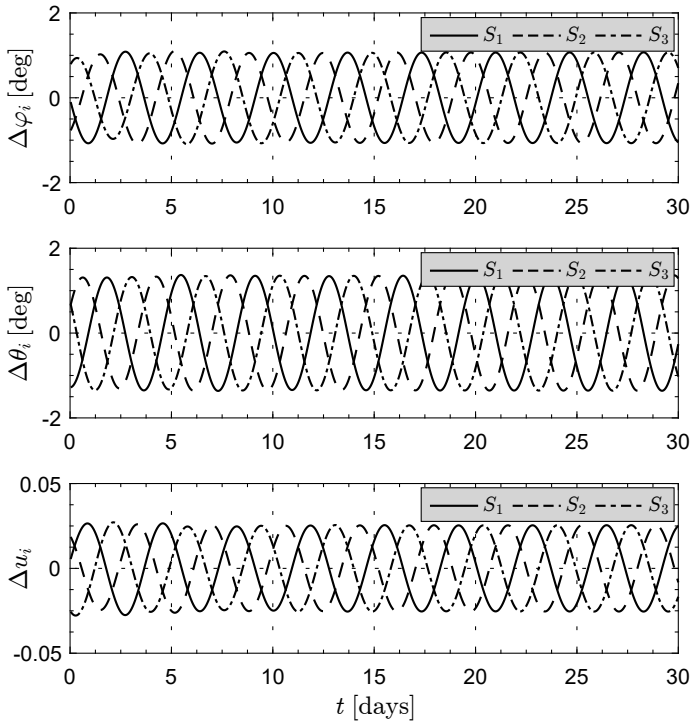

Figure 11: Control input with control law given by Eq. (35).

Because the relative velocity information is not incorporated into the feedback control system, $\mathbb{W}_v$ can be freely adjusted. Using a trial and error procedure, a satisfactory control performance is obtained when the parameters in Eq. (45) are chosen to be $\lambda_i^p = \lambda_i^v = 100$, $\mathbf{\Phi} = -18\,\mathbb{I}_3$, and $\mathbf{\Gamma} = 10\,\mathbb{I}_3$. Finally, since the initial value of intermediate variables $\boldsymbol{\xi}_i$ can be randomly chosen, here it is assumed that $\boldsymbol{\xi}_{i0} = \mathbf{0}$.

To illustrate the performance of the control law given by Eq. (45), the time histories of position and velocity errors are reported in Fig. 13 and Fig. 14, for a time interval of 30 days. Figures 15 and 16 illustrate the control input and the intermediate variables $\boldsymbol{\xi}_i$, while the instantaneous positions of the three deputies are shown in Fig. 17. Note that, even in absence of relative velocity measurements, the steady state errors of the three deputies all converge to zero, while consensus is guaranteed during the whole transition phase. When compared with the results of the full state feedback case, the control law given by Eq. (45) produces a more oscillating behavior and requires higher control inputs.

5. Conclusions

The problem of solar sail formation flying around a heliocentric displaced orbit has been investigated. Distributed architectures of the formation control system have been developed for both a full state feedback case and a relative velocity-free case, the latter being achieved with the introduction of a passive filter that removes the relative velocity requirement. In particular, the discussed consensus algorithms rely on a protocol that enables multiple solar sails to maintain a desired formation geometry, while every available neighbor-to-neighbor information coupling is used to obtain an asymptotic coordination.

Illustrative examples have shown that the proposed consensus-based strategies guarantee a time-balanced maneuver for solar sail formation flying around a displaced orbit. Compared with a traditional chief-deputy framework, the inclusion of the shared data flow among neighbors into cooperative control system improves the robustness and redundancy of the group, thus preventing an unfavorable situation in which a chief malfunction would imply a failure of the whole formation system.

A natural extension of this work is the analysis of the consensus algorithm performance when a non-ideal force model is assumed to describe the solar sail propulsive acceleration, or larger distances between satellites

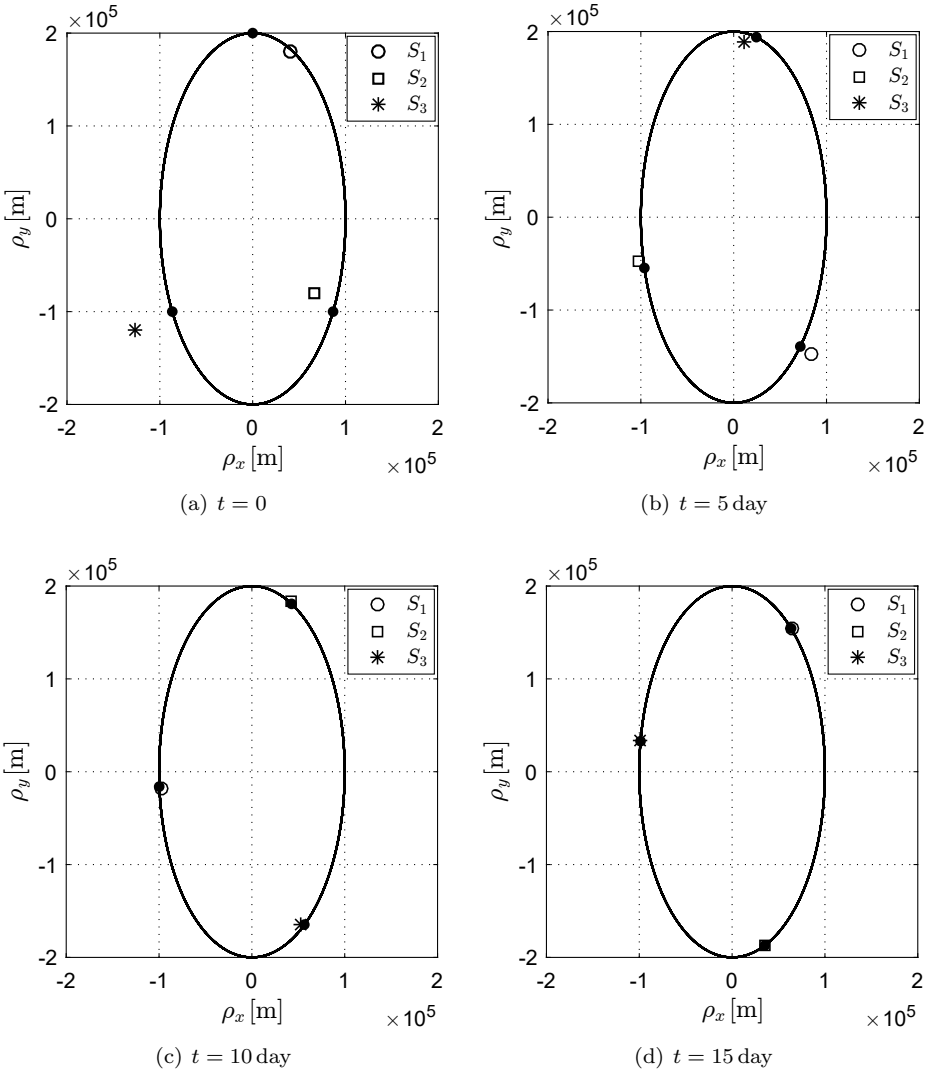

(a) $t = 0$ (b) $t = 5\,\text{day}$

(c) $t = 10\,\text{day}$ (d) $t = 15\,\text{day}$

Figure 12: Relative trajectories of the three deputies in the full state feedback case.

are considered (as for Earth remote sensing or space environment measurement). In this case, the control law design must be revised to deal with the thermo-optical characteristics of the reflective film and other constraints such as, for example, time delays and data package lost.

6. Acknowledgements

This work was supported by the National Natural Science Foundation of China (No. 11472213) and Chinese Scholarship Council.

References

[1] G. Vulpetti, L. Johnson, G. L. Matloff, Solar Sails: A Novel Approach to Interplanetary Travel, Springer-Verlag, New York, 2015, Ch. 9, pp. 83–101.

[2] G. Vulpetti, C. Circi, Mass breakdown model of solar-photon sail shuttle: The case for mars, Acta Astronautica 119 (2016) 87–100, doi: 10.1016/j.actaastro.2015.11.010.

[3] D. J. O'Shaughnessy, J. V. McAdams, P. D. Bedini, A. B. Calloway, K. E. Williams, B. R. Page, Messenger's use of solar sailing for cost and risk reduction, Acta Astronautica 93 (2014) 483–489, doi: 10.1016/j.actaastro.2012.10.009.

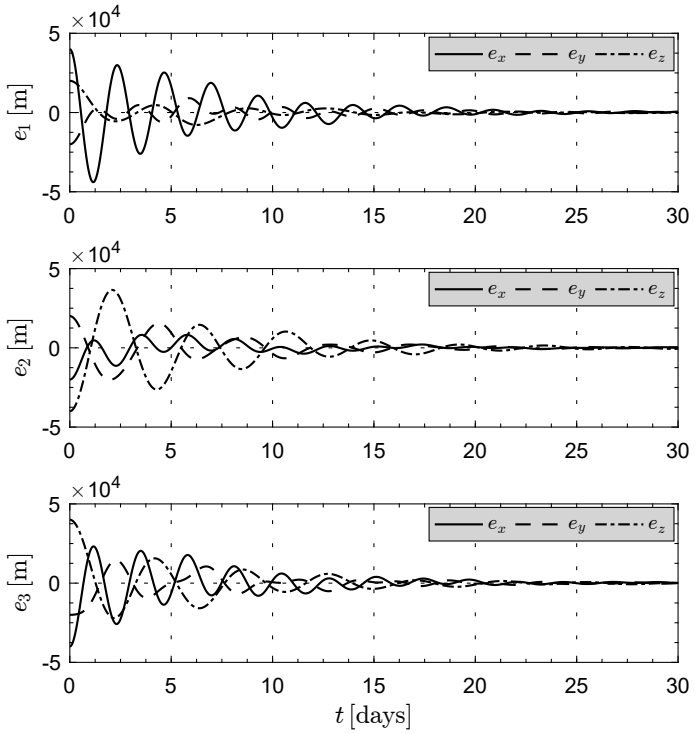

Figure 13: Components of the position errors in the relative velocity-free case.

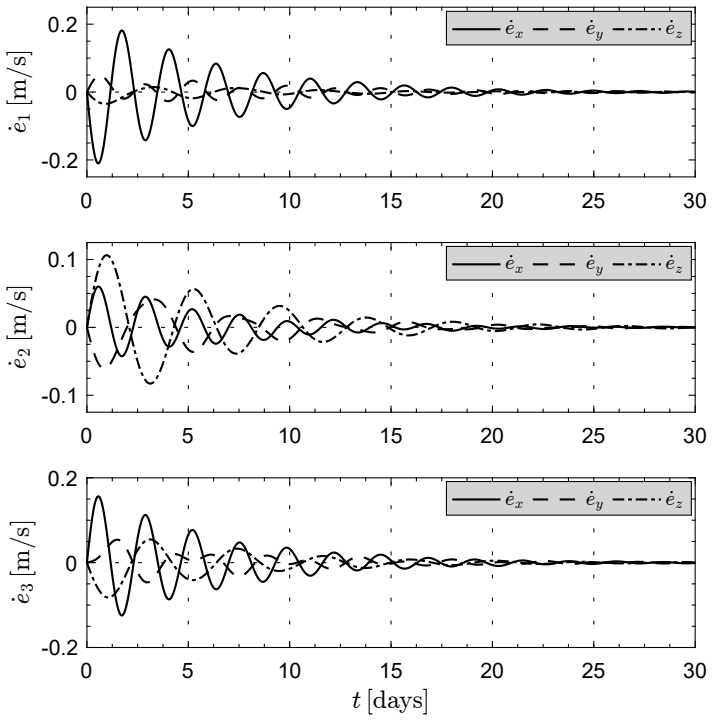

Figure 14: Components of the velocity errors in the relative velocity-free case.

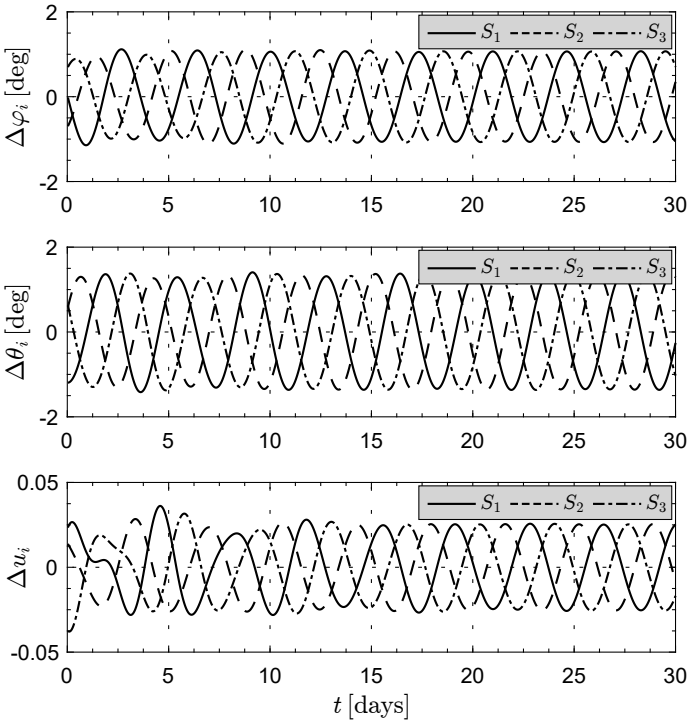

Figure 15: Control input with control law given by Eq. (45).

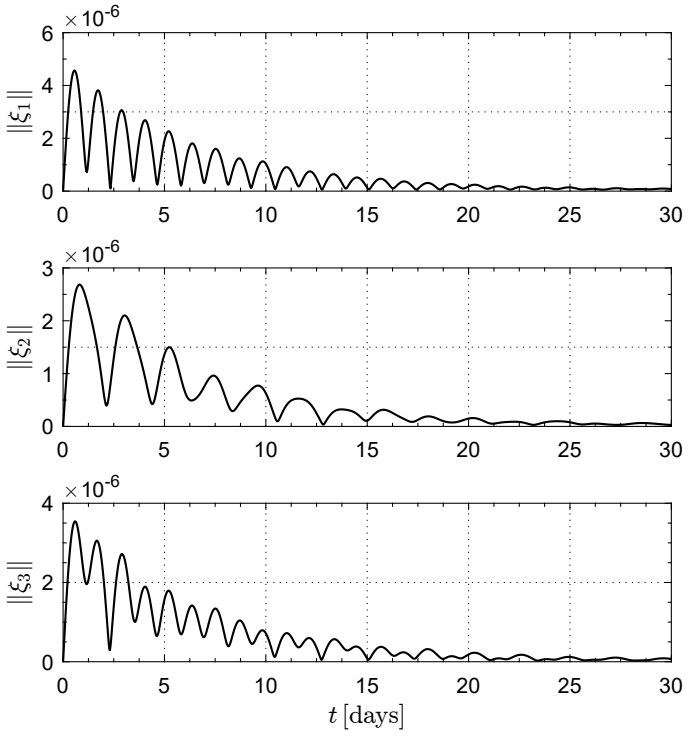

Figure 16: Variations of $\|\boldsymbol{\xi}_i\|$ in Eq. (43).

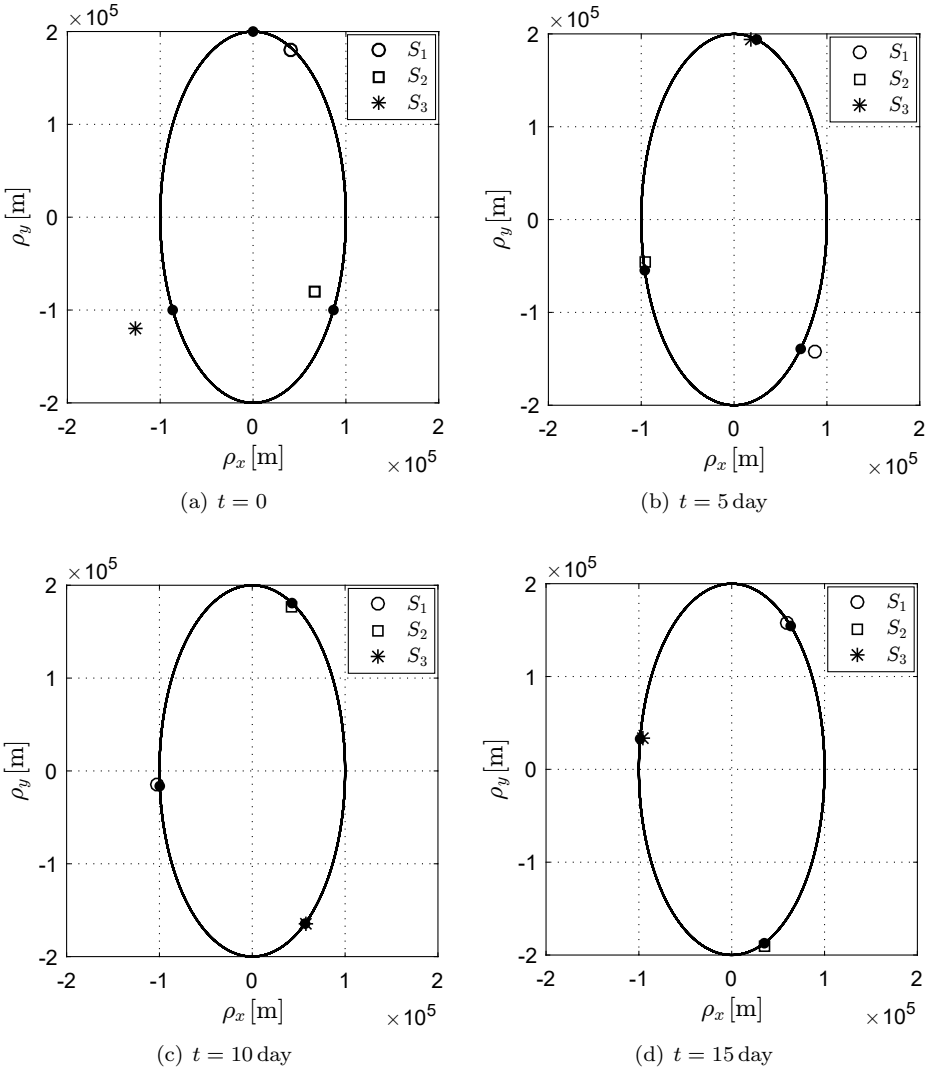

(a) $t = 0$ (b) $t = 5\,\text{day}$

(c) $t = 10\,\text{day}$ (d) $t = 15\,\text{day}$

Figure 17: Relative trajectories of the three deputies in the relative velocity-free case.

[4] A. A. Quarta, G. Mengali, Solar sail missions to mercury with venus gravity assist, Acta Astronautica 65 (3–4) (2009) 495–506, doi: 10.1016/j.actaastro.2009.02.007.

[5] M. Ceriotti, B. L. Diedrich, C. R. McInnes, Novel mission concepts for polar coverage: An overview of recent developments and possible future applications, Acta Astronautica 80 (2012) 89–104, doi: 10.1016/j.actaastro.2012.04.043.

[6] M. Ceriotti, C. R. McInnes, Hybrid solar sail and solar electric propulsion for novel earth observation missions, Acta Astronautica 69 (9-10) (2011) 809–821, doi: 10.1016/j.actaastro.2011.06.007.

[7] R. J. McKay, M. Macdonald, J. Biggs, C. R. McInnes, Survey of highly non-Keplerian orbits with low-thrust propulsion, Journal of Guidance, Control, and Dynamics 34 (3) (2011) 645–666, doi: 10.2514/1.52133.

[8] G. Mengali, A. A. Quarta, Optimal heliostationary missions of high-performance sailcraft, Acta Astronautica 60 (8-9) (2007) 676–683, doi: 10.1016/j.actaastro.2006.07.018.

[9] A. A. Quarta, G. Mengali, Solar sail capabilities to reach elliptic rectilinear orbits, Journal of Guidance, Control, and Dynamics 34 (3) (2011) 923–926, doi: 10.2514/1.51638.

[10] A. A. Quarta, G. Mengali, Optimal solar sail transfer to linear trajectories, Acta Astronautica 82 (2) (2013) 189–196, doi: 10.1016/j.actaastro.2012.03.005.

[11] C. R. McInnes, Passive control of displaced solar sail orbits, Journal of Guidance, Control and Dynamics 21 (6) (1998) 975–982, doi: 10.2514/2.4334.

[12] C. R. McInnes, Dynamics, stability, and control of displaced non-Keplerian orbits, Journal of Guidance, Control and Dynamics 21 (5) (1998) 799–805, doi: 10.2514/2.4309.

[13] H. Baoyin, C. R. McInnes, Solar sail halo orbits at the Sun-Earth artificial L_1 point, Celestial Mechanics and Dynamical Astronomy 94 (2) (2006) 155–171, doi: 10.1007/s10569-005-4626-3.

[14] K. Parsay, H. Schaub, Designing solar sail formations in sun-synchronous orbits for geomagnetic tail exploration, Acta Astronautica 107 (2015) 218–233, doi: 10.1016/j.actaastro.2014.11.018.
[15] M. Macdonald, C. R. McInnes, D. Alexander, A. Sandman, Geosail: Exploring the magnetosphere using a low-cost solar sail, Acta Astronautica 59 (8–11) (2006) 757–767, doi: 10.1016/j.actaastro.2005.07.023.
[16] S. Gong, H. Baoyin, J. Li, Solar sail formation flying around displaced solar orbits, Journal of Guidance, Control, and Dynamics 30 (4) (2007) 1148–1152, doi: 10.2514/1.24315.
[17] W. Wang, Y. Jianping, G. Mengali, A. A. Quarta, Invariant manifold and bounds of relative motion between heliocentric displaced orbits, Journal of Guidance, Control and Dynamics 39 (8) (2016) 1764–1776, doi: 10.2514/1.G001751.
[18] W. Ren, Formation keeping and attitude alignment for multiple spacecraft through local interactions, Journal of Guidance, Control, and Dynamics 30 (2) (2007) 633–638, doi: 10.2514/1.25629.
[19] W. Wang, G. Mengali, A. A. Quarta, J. Yuan, Formation flying for electric sails in displaced orbits. Part II: Distributed coordinated control, Advances in Space Research 60 (6) (2017) 1130–1147, doi: 10.1016/j.asr.2017.06.017.
[20] P. Janhunen, Electric sail for spacecraft propulsion, Journal of Propulsion and Power 20 (4) (2004) 763–764, doi: 10.2514/1.8580.
[21] P. Janhunen, Status report of the electric sail in 2009, Acta Astronautica 68 (5-6) (2011) 567–570, doi: 10.1016/j.actaastro.2010.02.007.
[22] G. Aliasi, G. Mengali, A. A. Quarta, Artificial lagrange points for solar sail with electrochromic material panels, Journal of Guidance, Control, and Dynamics 36 (5) (2013) 1544–1550, doi: 10.2514/1.58167.
[23] G. Mengali, A. A. Quarta, Heliocentric trajectory analysis of Sun-pointing smart dust with electrochromic control, Advances in Space Research 57 (4) (2016) 991–1001, doi: 10.1016/j.asr.2015.12.017.
[24] J. Mu, S. Gong, J. Li, Reflectivity-controlled solar sail formation flying for magnetosphere mission, Aerospace Science and Technology 30 (1) (2013) 339–348, doi: 10.1016/j.ast.2013.09.002.
[25] B. Dachwald, M. Macdonald, C. R. McInnes, G. Mengali, A. A. Quarta, Impact of optical degradation on solar sail mission performance, Journal of Spacecraft and Rockets 44 (4) (2007) 740–749, doi: 10.2514/1.21432.
[26] B. Dachwald, G. Mengali, A. A. Quarta, M. Macdonald, Parametric model and optimal control of solar sails with optical degradation, Journal of Guidance, Control, and Dynamics 29 (5) (2006) 1170–1178, doi: 10.2514/1.20313.
[27] L. Niccolai, A. A. Quarta, G. Mengali, Electric sail elliptic displaced orbits with advanced thrust model, Acta Astronautica 138 (2017) 503–511, doi: 10.1016/j.actaastro.2016.10.036.
[28] W. Wang, G. Mengali, A. A. Quarta, J. Yuan, Formation flying for electric sails in displaced orbits. Part I: Geometrical analysis, Advances in Space Research 60 (6) (2017) 1115–1129, doi: 10.1016/j.asr.2017.05.015.
[29] W. Ren, R. W. Beard, E. M. Atkins, Information consensus in multivehicle cooperative control, IEEE Control Systems Magazine 27 (2) (2007) 71–82, doi: 10.1109/MCS.2007.338264.
[30] A. R. Mehrabian, S. Tafazoli, K. Khorasani, Cooperative tracking control of Euler-Lagrange systems with switching communication network topologies, in: IEEE/ASME International Conference on Advanced Intelligent Mechatronics, Montreal (Canada), 6–9 July 2010, doi: 10.1109/AIM.2010.5695803.
[31] W. Ren, E. Atkins, Distributed multi-vehicle coordinated control via local information exchange, International Journal of Robust and Nonlinear Control 17 (11) (2007) 1002–1033, doi: 10.1002/rnc.1147.
[32] W. Ren, Distributed leaderless consensus algorithms for networked Euler-Lagrange systems, International Journal of Control 82 (11) (2009) 2137–2149, doi: 10.1080/00207170902948027.
[33] J. E. Slotine, W. Li, Applied nonlinear control, NJ: Prentice-Hall, New York, 1991, pp. 124–128.